

SCPMan: Shape Context and Prior Constrained Multi-scale Attention Network for Pancreatic Segmentation*

1st Leilei Zeng
College of Computer Science and
Software Engineering
Shenzhen University
Shenzhen, China
zengleilei123@gmail.com

2nd Xuechen Li
College of Computer Science and
Software Engineering
Shenzhen University
Shenzhen, China
timlee@szu.edu.cn

3rd Xinquan Yang
College of Computer Science and
Software Engineering
Shenzhen University
Shenzhen, China
xinquanyang99@gmail.com

4th Linlin Shen
College of Computer Science and
Software Engineering
Shenzhen University
Shenzhen, China
llshen@szu.edu.cn

5th Song Wu
South China Hospital
Medical School
Shenzhen University
Shenzhen, China
wusong@szu.edu.cn

Abstract—Due to the poor prognosis of Pancreatic cancer, accurate early detection and segmentation are critical for improving treatment outcomes. However, pancreatic segmentation is challenged by blurred boundaries, high shape variability, and class imbalance. To tackle these problems, we propose a multi-scale attention network with shape context and prior constraint for robust pancreas segmentation. Specifically, we proposed a Multi-scale Feature Extraction Module (MFE) and a Mixed-scale Attention Integration Module (MAI) to address unclear pancreas boundaries. Furthermore, a Shape Context Memory (SCM) module is introduced to jointly model semantics across scales and pancreatic shape. Active Shape Model (ASM) is further used to model the shape priors. Experiments on NIH and MSD datasets demonstrate the efficacy of our model, which improve the state-of-the-art Dice Score for 1.01% and 1.03% respectively. Our architecture provides robust segmentation performance, against the blurry boundaries, and variations in scale and shape of pancreas.

Index Terms—Medical Image Segmentation, Activate Shape Model

I. INTRODUCTION

Pancreatic cancer is one of the most lethal malignancies with an inferior prognosis and a 5-year survival rate of less than 9%. Therefore accurate early detection and appropriate treatment play a critical role in improving its prognosis [1], [2]. Accurate segmentation of pancreatic images as a prerequisite for detecting pancreatic cancer, can effectively eliminate interferences of complex background and benefit physicians for accurately assessing disease progression and treatment response. Computed tomography (CT) can clearly show the structure of the pancreas and is the most widely used

examination method for pancreatic cancer detection by clinical imaging physicians [3]–[5]. However, manually outlining the pancreas is very tedious, time-consuming, and unable to meet clinical needs. Therefore there is an urgent need for a system that can automate the segmentation of the pancreas, which can help imaging physicians to conduct early screening and quantitative detection of pancreatic lesions.

Different from other abdominal organs, such as the liver [6], lung [7], and kidney [8], which can be effectively segmented by AI-based system, the segmentation accuracy of the pancreas is not high enough to be applied to clinical practise, due to the following challenges: 1) Unclear boundaries. The boundary of the pancreas cannot be well defined due to the problem of fuzzy boundary perturbation caused by the similar density of pancreas and the surrounding tissues (e.g., stomach wall, duodenum, small intestine). 2) High variability in shape. The shape, size, and location of the pancreas varies greatly across individuals. This makes it difficult for artificial intelligence (AI) to represent its shape and location. 3) The pancreas occupies only a small portion of the entire CT image. There is a serious imbalance between size of the target and the background, which leads to overfitting problem on the background region.

Given these challenges, traditional machine learning image segmentation algorithms struggle to accurately delineate pancreatic boundaries where the edges are unclear [9], [10]. The same problem happens in natural segmentation when the boundaries are blurred or ambiguous [11], [12]. Prior works [13], [14] exploit multi-scale features to address, blurred boundaries by fusing cross-scale representations. In pancreas segmentation, the combination of multi-scale features also

Corresponding author: Linlin Shen and Song Wu.

achieves promising performance [15], [16]. However, pancreas segmentation presents challenges beyond boundary ambiguity. Unlike other abdominal organs (e.g. kidney, liver) with relatively fixed morphology, the pancreas exhibits high variability in shape across individuals. The irregular shape and complex morphology of the pancreas lead to difficulties and poor robustness in modeling its shape representations. Li et al. [17] proposed to use attentional mechanisms and multi-scale convolution to enrich contextual information and prevent the learning of irrelevant regions, which reduced the impact of inter-class similarity, and achieved 86.10% Dice Score on the NIH dataset. Davradou.A [18] proposed to solve the pancreas segmentation problem by applying a modified U-Net model to the cropped data, based on a morphological active contour algorithm. However, its Dice score is relatively low, which is only 67.67%. Yu et al. [19] proposed a recurrent saliency transformation network [20], which allowed the network to be jointly optimized as well as propagate multi-stage visual information to improve segmentation accuracy. Boundary ambiguity and high shape variability, which are intrinsic characteristics of the pancreas, are main challenges for localization and segmentation. However, previous approaches either ignore or fail to effectively model these properties. Prior arts tackling shape variation or boundary ambiguity demonstrate limited performance [15]–[17], and two-step approach e.g. like [18] is more complex and resource-consuming.

In this work, we propose a hybrid multi-scale attention shape context memory and an ASM (Activate Shape Model) prior constraint based pancreas segmentation network, to address both blurred pancreas boundaries and large shape variations problems. The main contributions of this is work are:

- A Multi-scale Feature Extraction Module (MFE) and a Mixed-scale Attention Integration Module (MAI) are introduced to pancreas segmentation to tackle the issues of blurred pancreas boundaries.
- A shape context memory (SCM) module is proposed to jointly model pancreas location and shape representation.
- An ASM prior constraint module is developed to guide pancreas shape modeling to provide shape priors.
- A weighted binary cross-entropy (BCE) and an Iou loss function are used to address the imbalance problem between the size of background and pancreas.

II. RELATED WORK

In the previous subsections, the significance and difficulties of pancreas segmentation studies were summarized and presented. In the next subsections, the process of pancreas segmentation studies is reviewed in detail. The rapid development of deep learning has led to an explosion of techniques for pancreas segmentation in abdominal CT scans. This segmentation can be divided into traditional machine learning methods and deep learning-based methods.

A. Traditional machine learning methods

In traditional machine learning, heuristic methods, such as the approach developed by Tam et al. [21], involve selecting seed points within the pancreas and using region growing techniques for segmentation. Shan et al. [22] segment the pancreas by distinguishing it from surrounding tissues using Otsu [23] threshold algorithms and morphological operations. However, these methods rely heavily on the selection of threshold ranges and are often challenged by subtle density differences between the pancreas and adjacent tissues, leading to potential inaccuracies. To address these limitations, researchers including Erdt [24] and Karasawa [25] et al. have developed more effective graph-based algorithms, although these algorithms still introduce considerable human generalization bias and rely on manual feature intervention, limiting their applicability for automated segmentation.

B. Deep learning based methods

In the field of deep learning, the success of these techniques in natural image processing has stimulated their application in medical image analysis [26]–[28]. Deep learning-based pancreas segmentation aims to mitigate the generalization bias inherent in traditional methods. These methods are mainly divided into two categories: convolutional neural network (CNN)-based and transformer-based methods. Take Zhou et al. [28] as an example, a CNN-based approach employs a full convolutional network (FCN) fixed-point model to improve iterative accuracy in small organ segmentation. Li et al. [20] proposed an advanced pancreas segmentation model combining a dual adversarial network and a pyramid pool module, achieving a Dice coefficient of $83.31 \pm 6.32\%$. Furthermore, Li et al. [29] enhanced the U-Net model using a multi-scale attention-dense residual U-net (MAD-UNet), resulting in more accurate feature acquisition and a Dice coefficient of $86.10 \pm 3.52\%$ on the NIH dataset. Yu et al. [17] proposed a multi-stage saliency segmentation approach, using the segmentation mask of the current stage to improve the input of subsequent stages. However, the limited receiving range of CNNs hinders their focus on distant regions and to some extent ignores rich global context information, making it difficult to further optimize network performance. To overcome these limitations, transformer-based approaches have been developed. Qiu et al. [?] introduced residual transformer UNet (RTUNet) for pancreas segmentation, achieving a Dice similarity coefficient of $86.25 \pm 4.52\%$ on the NIH dataset. Dai et al. [?] proposed a two-stage trans-deformer network, merging 2D Unet, deformable convolution, and wavelet-based multi-input module, showing excellent performance on both the NIH and MSD datasets. In addition, Zhu et al. [?] recognized the 3D nature of CT data and explored the effectiveness of 3D networks, achieving a dice coefficient of $84.59 \pm 4.86\%$ on the NIH dataset. Zhang et al. [19] developed a segmentation framework that combined multi-spectral registration with 3D level set techniques to refine probabilistic graphs to improve pancreatic edge prediction accuracy, achieving a dice coefficient of 84.47

$\pm 4.36\%$ on the NIH dataset. However, Transform-based approaches usually require a two-stage approach because initial localization of the pancreatic region is required first, while the extensive GPU memory requirements of 3D networks usually lead to CT scans being segmented into smaller portions or processed at reduced resolution, limiting spatial context learning. Therefore, developing a network that can effectively utilize the context relationship of pancreatic CT sequences in a single stage is crucial for accurate pancreatic segmentation.

III. METHODS

In this work, a shape context and prior constrained multi-scale attention Network is proposed for the key challenges in pancreas segmentation i.e., blurred boundary, various shape and unbalanced foreground and background. As shown in Fig. 1 for blurred boundaries, we design a Multi-scale Feature Extraction (MFE) module and a Mixed-scale Attention Integration (MAI) module, inspired by camouflage detection [13]. For shape modeling, we incorporate anatomical priors through a Shape Context Memory (SCM) module to implicitly guide location and shape prediction, as well as an ASM Prior Constraint module for explicit shape regularization. Finally, we handle class imbalance using weighted BCE and IoU losses.

A. Multi-scale Feature Extraction Module.

The multi-scale feature extraction module consists of a feature extractor and a feature compressor (Fig. 2). The proposed feature extractor module adopts ResNet-50 [30] as the backbone, but removes the FC layer after the last ResNet block. We take the feature maps before the first max pooling as " L_1 ", term the remaining layers as " L_2 " to " L_5 " corresponding to ResNet blocks 1-4. To match UNet++ input size, the five extracted features are fed into feature compressor module, using simplified ASPP [31] for " L_5 " and CBR (include Conv-BatchNorm-Relu) for " L_{1-4} ".

$$F_i^d = MFE(I^d), d \in [0.5x, 1.0x, 1.5x], i \in [1, 2, 3, 4, 5] \quad (1)$$

where $I^d \in \mathbb{R}^{H \times W \times 3}$ is the input, including 3 different scales, F_i^d is the output Multi-scale features.

B. Mixed-scale Attention Integration Module.

The scale-space theory, which uses image and feature pyramids to construct features integrating multi-scales and semantics, has been widely and effectively applied in natural images to deepen the model's multi-scale structural understanding [32]–[35]. Influenced by [13], we use the Mixed-scale Attention Integration (MAI) module (e.g., Fig. 3) to solve the problem of feature fusion at different scales.

Specifically, we take the feature F_i^d extracted by MFE module and use MAI module to integrate F_i^d to the 1.0x scale (F_i). The processing flow is shown in Algorithm 1.

F_i^d denotes the multi-scale features, where M is max pooling, A is average pooling, and B is bilinear interpolation. We integrate the features to 1.0x scale using the proposed MAI module, which consists of downsample, upsample and

Algorithm 1 MAI Processing

Input: F_i^d : The multi-scale feature from MFE module, $i \in [1, 2, 3, 4, 5]$, $d \in [0.5 \times, 1.0 \times, 1.5 \times]$

Output: F_i : The integrated feature

- 1: $F_i^{down} = CBR([M(F_i^{1.5 \times}) + A(F_i^{1.5 \times})])$
 - 2: $F_i^{up} = CBR([B(F_i^{0.5 \times})])$
 - 3: $F_i^{ori} = CBR(F_i^{1.0 \times})$
 - 4: $F_i = Concat(F_i^{down}, F_i^{ori}, F_i^{up})$
 - 5: $F_{i_att}^{0.5 \times}, F_{i_att}^{1.0 \times}, F_{i_att}^{1.5 \times} = AG(F_i)$
 - 6: $F_i = F_{i_att}^{0.5 \times} \times F_i^{0.5 \times} + F_{i_att}^{1.0 \times} \times F_i^{1.0 \times} + F_{i_att}^{1.5 \times} \times F_i^{1.5 \times}$
 - 7: **Return** F_i
-

CBR ("Conv-BN-ReLU") and CBS ("Conv-BN-Split") layers. Specifically, F_i^{down} , F_i^{up} and F_i^{ori} are the intermediate features after downsample, upsample and CBR operations, respectively. The final integrated features are computed by weighted sum of the attention-modulated multi-scale features after the AG operations.

C. Shape Context Memory Module

CT sequences exhibit continuity in organ shape and appearance across slices. Therefore, we propose a shape context memory (SCM) module to improve contextual feature learning. The high variability in pancreas shape, size and location makes big challenges for direct localization in individual slices. In contrast, our SCM module is designed to model contextual information of the entire image sequence, encoding the average spatial location and shape of the pancreas. This representation helps to guide accurate localization and shape modeling of the pancreas within the abdomen. We cache intermediate features from the outputs of MAI 2-5 with a batch of N slices. To minimize redundancy, the cached features are weighted by their contributions for subsequent pancreas segmentation, i.e. useful cached slices receive higher weights. The cached features are finally concatenated and fed into the decoder. This process can be formulated as:

$$\begin{aligned} T_{cs} &= CS([T_1, T_2 \dots T_n]), T_{cs} \in \mathbb{R}^{1 \times N \times H \times W} \\ M_i &= WB(T_{cs}), M_i \in \mathbb{R}^{1 \times N \times H \times W} \end{aligned} \quad (2)$$

WB and CS denote the "Memory Weighted Block" and "Channel Squeeze" in Fig. 4.

D. Segmentation Module

We adopt UNet++ [36] as segmentation module, with some modification in the encoding stage. Rather than down-sampling to derive multi-scale features, we directly extract UNet++ input features at different scales from the output of the MAI module. In the decoding stage, we concatenate the shape context features M_i learned from the SCM module with the output features F_i of the MAI module to obtain N_i , which is then used for upsampling to derive the final segmentation result. The formal expression of this process is formula 3.

$$N_i = Concat(F_i, M_i), N_i \in \mathbb{R}^{N \times C \times H \times W} \quad (3)$$

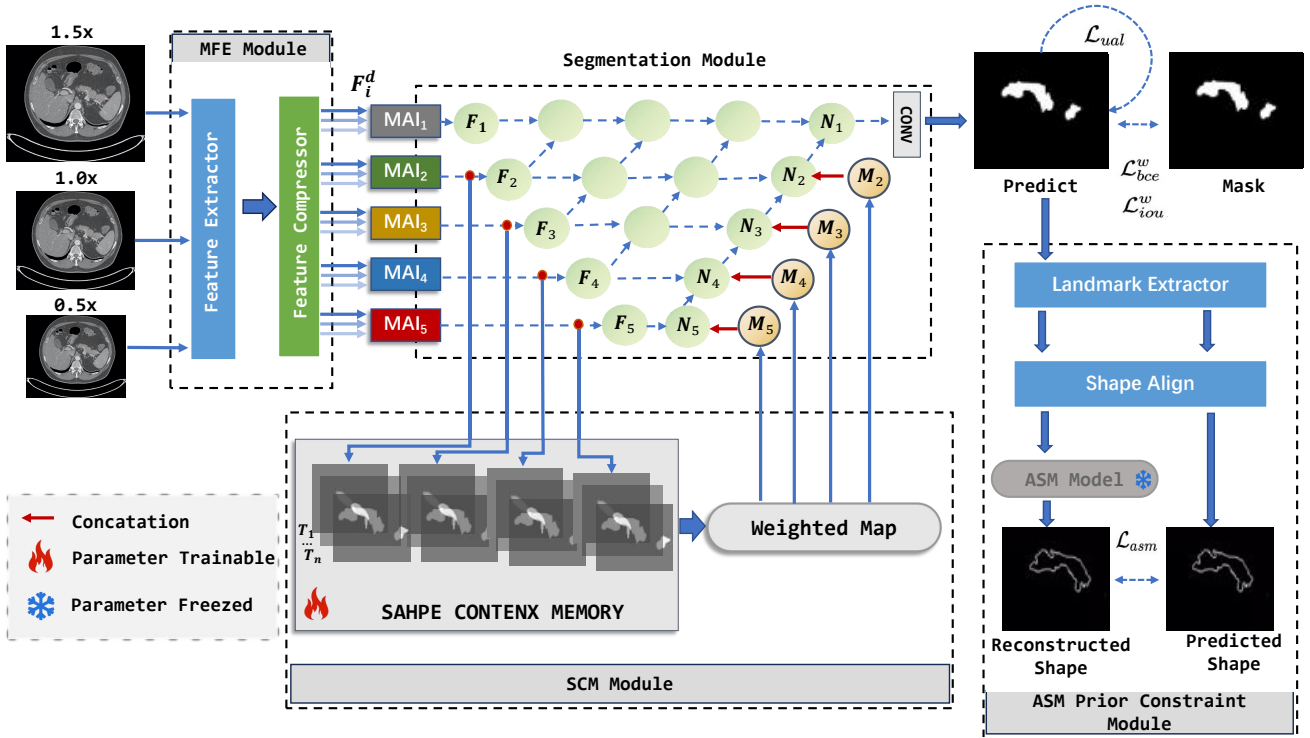


Fig. 1. The architecture of our proposed network. Firstly, a Multi-scale Feature Extractor (MFE) module is designed to extract the multi-scale feature (F_i^d). Successively, a Mixed-scale Attention Integration (MAI) module is designed to integrate the multi-scale feature F_i^d to 1.0x (F_i). More, Shape Context Memory (SCM) module is designed to enhance the network’s ability to model the shape and location of the pancreas and generate the enhanced feature M_i . Finally, the concatenated feature $N_i = [F_i, M_i], i \in [2, 3, 4, 5]$ are fed to the Unet++ decoder for mask generation.

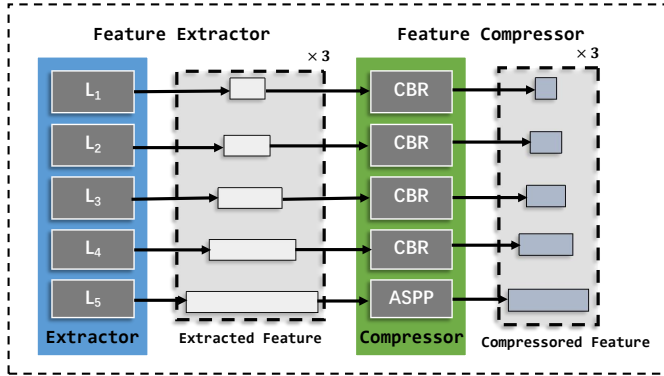


Fig. 2. Multi-scale Feature Extraction (MFE) Module. The MFE module consists of two main components: a feature extractor and a feature compressor, the feature extractor mainly uses the structure of Resnet-50, and the feature compressor uses CBRs for compression (the last layer of feature uses ASPP), and finally output the multi-scale features F_i^d .

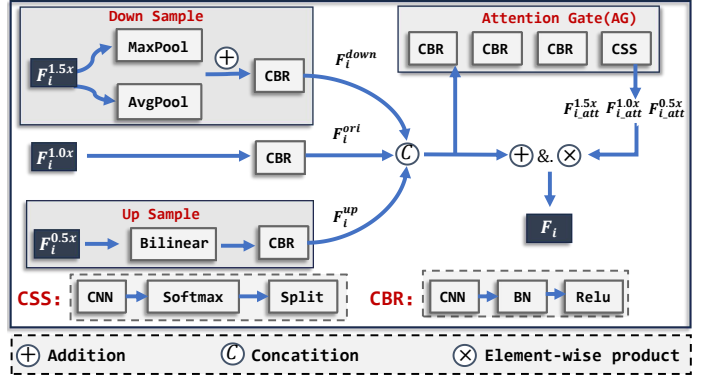


Fig. 3. Mixed-scale Attention Integration (MAI) Module. MAI module takes as input the MFE output features $F_i^d, i \in [1, 2, 3, 4, 5], d \in [0.5 \times, 1.0 \times, 1.5 \times]$ of the MFE, and generate the integrated multi-scale features F_i .

E. ASM Prior Constraint module

We further improve pancreas shape modeling by incorporating anatomical shape priors through ASM constraints. Specifically, we firstly construct an ASM model with a shape prior constraints based on representative pancreatic shape features. The ASM model is trained as described in Algorithm 2, and its output mean shape \bar{s} and shape prior P are used by Algorithm 3 to reconstruct the shape of predicted mask. When

applying the trained ASM model for shape regularization in our proposed network, thresholding is performed on the predicted pancreas masks to remove small region to avoid the problems that prediction maps contain multiple regions. The largest region with size greater than the threshold is selected. Based on typical pancreas size, the threshold is set as 50 pixels. The resulting \mathcal{L}_{asm} term, calculated as the MSE between the reconstructed shape (S') and predicted mask (S_0) output by Algorithm 3, is incorporated into the final loss. The approach

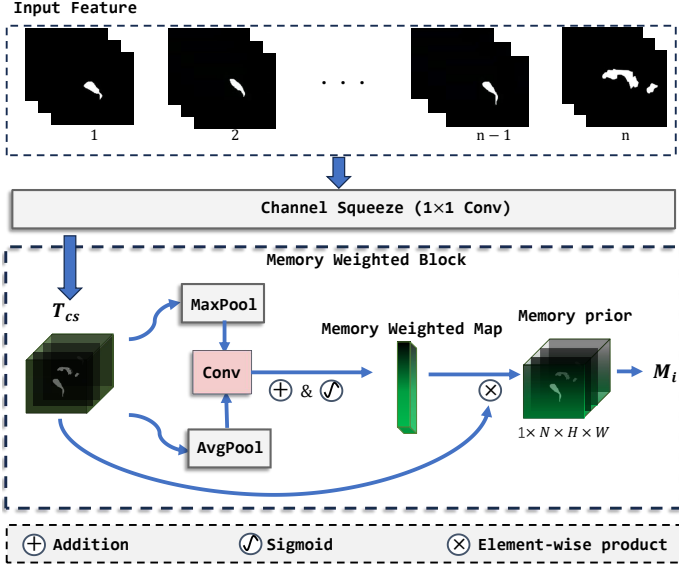


Fig. 4. Shape Context Memory (SCM) Module.

Algorithm 2 ASM Training

Input: $I = I_1, I_2, \dots, I_N$: Sample training images

Output: \bar{s} : Mean Shape P : Shape Prior b : Shape Deforms

1: Locate landmarks s_i from I_i using sobel and interpolation algorithm

$$s_i = [x_1, y_1, \dots, x_n, y_n], s_i \in \mathbb{R}^{2n \times 1}, n = 238$$

2: Align all landmarks $S = s_1, s_2, \dots, s_N$

3: Calculate the average shape $\bar{s} = \frac{1}{N} \sum_{i=1}^N s_i$

4: Construct the shape difference matrix $D = S - \bar{s}$

5: Build the covariance matrix: $C = D^T D$

6: Use PCA (Principal Component Analysis) analysis to obtain shape prior P and deform coefficients b

$$P, b \leftarrow PCA(C)$$

7: **Return:** \bar{s}, P, b

Algorithm 3 ASM Based Shape Reconstruction

Input: M : Predicted mask \bar{s} : Mean Shape P : Shape Prior

Output:

S' : The Reconstructed Shape S_0 : Shape of the Predicted Mask

1: Choose the largest $area > threshold$ as $M_{largest}$ from M

2: Locate landmarks S_0 from $M_{largest}$ using sobel and interpolation algorithm

$$S_0 = [x_1, y_1, \dots, x_n, y_n], S_0 \in \mathbb{R}^{2n \times 1}, n = 238$$

3: Align S_0 to \bar{s}

4: Compute deform parameters b

$$b = P^T \times (S_0 - \bar{s}), P \in \mathbb{R}^{2n \times 9}, b \in \mathbb{R}^{9 \times 1}$$

5: Reconstruct shape S'

$$S' = \bar{s} + Pb, S' \in \mathbb{R}^{2n \times 1}$$

6: **Return:** S', S_0

Algorithm 4 L_{asm} Calculation

Input:

M : Predicted mask R : Shape Reconstruction (Algorithm 3) \bar{s} : Mean Shape P : Shape Prior

Output:

\mathcal{L}_{asm} : The ASM Loss

1: Generate reconstructed shape S' and predicted mask shape S_0

$$S', S_0 \leftarrow R(M, \bar{s}, P)$$

2: $\mathcal{L}_{asm} = MSE(S', S_0)$

3: **Return:** \mathcal{L}_{asm}

is summarized in Algorithm 4.

F. Loss Formulation

In the proposed model, the total training loss consists of four sub-losses:

$$\mathcal{L}_{total} = \mathcal{L}_{Iou}^w + \mathcal{L}_{BCE}^w + \mu \times \mathcal{L}_{ual} + \tau \times \mathcal{L}_{asm} \quad (4)$$

where \mathcal{L}_{Iou}^w and \mathcal{L}_{BCE}^w represent the weighted IoU loss and binary cross entropy (BCE) loss, respectively, which have been widely adopted in segmentation tasks to imbalanced foreground and background problems. We use the same definitions as [37]–[39], since their effectiveness has been validated in these works. In this work, \mathcal{L}_{ual} [13] is employed to further optimize the segmentation for blurred edges that are difficult to define, which is formulated as $\mathcal{L}_{ual}^{i,j} = 1 - |2M_{i,j} - 1|^2$ and the $M_{i,j}$ denote the predicted value at position (i, j) . Where μ is the \mathcal{L}_{ual} balance coefficient. Following previous work [13], we use the best equilibrium coefficient strategy cosine as the equilibrium coefficient strategy in this paper. The \mathcal{L}_{asm} is the ASM prior constraints loss and τ is the balance coefficient.

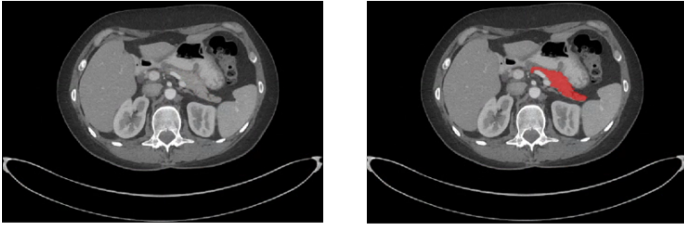
IV. EXPERIMENTS

A. Datasets and Evaluation Metrics

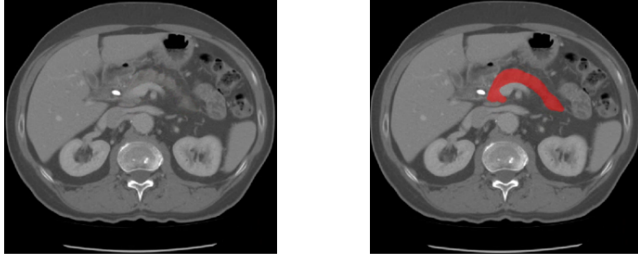
Datasets. We conducted experiments on two publicly available pancreas segmentation datasets: 1) NIH dataset: which consists of 82 abdominal contrast-enhanced CT scans from the National Institutes of Health (NIH) Clinical Center pancreas segmentation dataset [40], 2) MSD dataset: which consists of 281 labeled pancreas and pancreatic tumors from the Medical Segmentation Decathlon (MSD) Challenge pancreas segmentation dataset [5]. Examples of images from these two datasets with their corresponding labels are visualized in Fig. 5.

For each CT Volume in the NIH dataset, the volume size is $[512 \times 512 \times D]$, where $D \in [181, 466]$ is the number of slices along the transverse plane. The slice thickness of the CT scans varies from 1.5 mm to 2.5 mm, depending on the scan depth. We follow the principle of four-fold cross-validation and randomly divide the NIH dataset into four fixed subsets, which include 21, 21, 20, and 20 samples, respectively.

For each CT Volume in the MSD dataset, the volume size is $[512 \times 512 \times D]$, where $D \in [37, 751]$ is the number of slices along the transverse plane. Following previous work [34] on the MSD dataset, we combine the pancreas and pancreatic



(a) NIH Dataset Sample



(b) MSD Dataset Sample

Fig. 5. Example images in NIH dataset and MSD dataset.

tumor into a single entity as the segmentation target. We divide the dataset into four subsets containing 70, 70, 70, and 71 CT volumes respectively, for cross-validation.

Data preprocessing. In medical imaging, especially in computed tomography (CT) scans, choosing the best range of CT values is crucial to obtain clear and accurate images. For the specific case of pancreatic imaging, as a rule of thumb, we limit CT values to the range as a means of preconditioning. This specific range was identified as significantly enhancing the contrast in areas associated with the pancreas.

Evaluation Metrics. Dice score, Precision, and Recall are employed as the evaluation criteria. The definitions of the above three evaluation criteria are as follows:

$$Precision = \frac{TP}{TP + FP} \quad (5)$$

$$Dice = \frac{2TP}{2TP + FP + FN} \quad (6)$$

$$Recall = \frac{TP}{TP + FN} \quad (7)$$

Here TP, FP and FN represent True positive, False positive and False Negative.

B. Implementation Details

SGD with a momentum of 0.9 and a weight decay of 0.0005 is employed as the optimizer. The learning rate is initialized to 0.05 and follows a linear warm-up and decay schedule. The entire model is trained end-to-end on Tesla V100 GPU for 40 epochs with a batch size of 16. The number of cached Shape Context Memory features is kept the same as the batchsize during training. For data augmentation, random flipping and

rotation are applied to the training data. During inference, if the input size is smaller than the batchsize, we crop the Shape Context Memory features accordingly to match the input size before fusing them in the UNet++ segmentation module.

TABLE I
ABLATION STUDY OF THE PROPOSED MODULES ON THE NIH.

Baseline		SCM	\mathcal{L}_{asm}	DSC(%)
MFE	MAI			
✓				83.12
✓	✓			84.44
✓	✓		✓	86.14
✓	✓	✓		89.50
✓	✓	✓	✓	91.00

C. Ablation study

Table I demonstrates the individual contributions of our key components, a) MFE: the multi-scale feature extractor module; b) MAI: the mixed-scale attention integration module; c) Baseline: Only MFE and MAI components are used; d) SCM: the shape context memory module; e) \mathcal{L}_{asm} : The ASM prior constraint module.

Our baseline without the proposed SCM and ASM components achieves 84.44% Dice score on pancreas segmentation. As proposed in Table I, both the SCM and ASM components improve the segmentation performance of the baseline, e.g. SCM boosts Dice by 5% and ASM boosts by 2%. Combining SCM and ASM components leads to a 7% performance gain over the baseline, demonstrating the efficiency and complementarity of the proposed modules. The ablation study thus validates the contributions of our shape context memory module and ASM prior constraint model regularization.

Fig. 6 visualizes the segmentation improvements from adding different components. The MAI and MFE modules would reasonably segment regions with indistinct boundaries, ensuring a complete delineation of the pancreatic shape. The ASM prior constraint produces anatomically plausible pancreas shapes. The SCM module effectively captures shape contextual information to implicitly localize the pancreas. ASM and SCM modules complement each other, i.e. the joint model significantly improved segmentation than separate module. Qualitatively, the full model explores the benefits of both shape and context modeling, validating the design of our hybrid architecture. In Fig. 6 the red circles represent locations with significant differences.

Shape Context Memory for different Features. In order to verify which features should be cached in the memory caching to have a better and more positive impact on the final results, we conducted experiments on the cached features in the shape context memory module. The performance of different features for the final segmentation is shown in Table II. The experimental results show that when using the $F_2 - F_5$ feature extracted by MAI for shape contextual feature learning, the network shows the best segmentation performance.

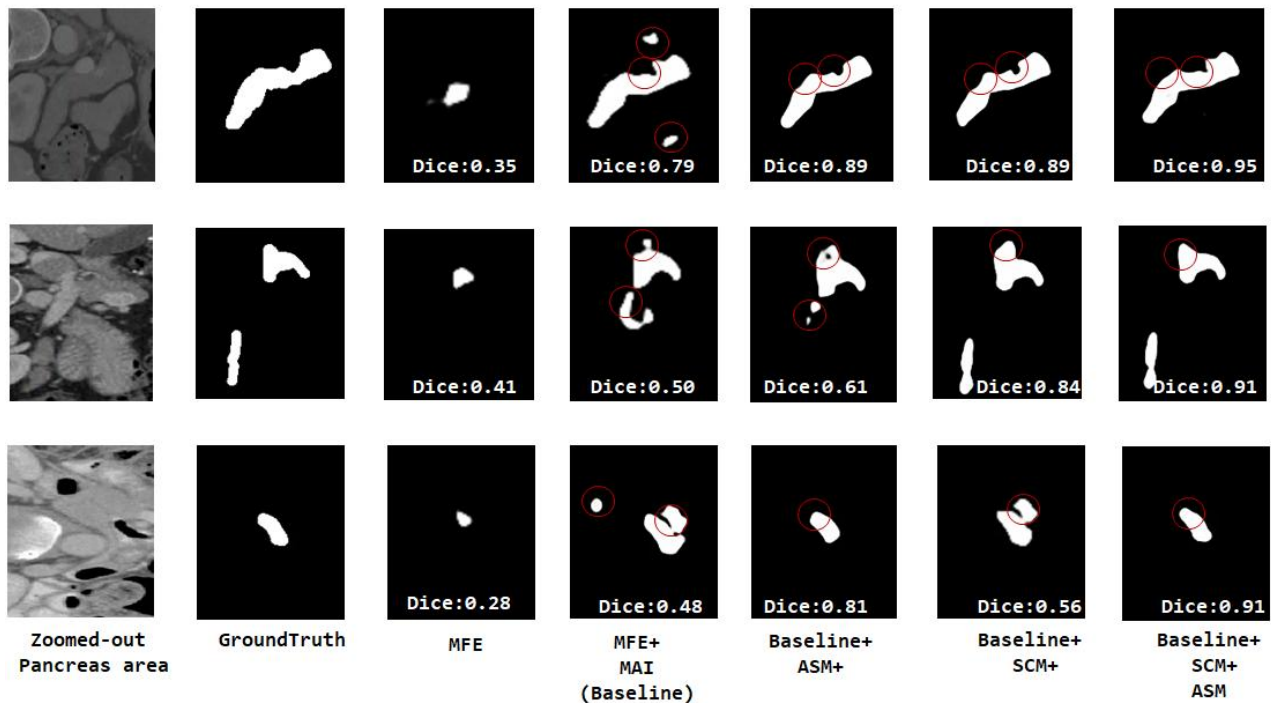


Fig. 6. Visualizes the segmentation improvements from adding different components.

TABLE II
ABLATION STUDY OF THE PROPOSED SCM MOUDLE ON THE NIH.

F_1	F_2	F_3	F_4	F_5	DSC(%)
			✓	✓	86.61
		✓	✓	✓	87.73
	✓	✓	✓	✓	89.50
✓	✓	✓	✓	✓	88.67

Including F_i from " L_1 " of the MAI module degrades performance, as the shallow features lack semantic information.

TABLE III
EFFECTIVENESS OF MODELING ASM USING DIFFERENT DATASET.

		Test	
		NIH	MSD
Train	NIH	86.14	88.32
	MSD	85.14	89.09
	—*	84.44	87.71

* "—" denotes baseline network without \mathcal{L}_{asm} .

ASM learning using different Dataset. We verified the effect of ASM models trained on different datasets, in terms of segmentation performanc. As shown in Table III, when employing \mathcal{L}_{asm} , the network achieves better segmentation performance than baseline network on both datasets, which demonstrates the effectiveness of \mathcal{L}_{asm} . It is noticed that

the ASM prior constraint module shows good cross-dataset performance. The module trained using NIH and MSD dataset achieve 0.6% and 0.7% higher Dice on MSD and NIH dataset, respectively, than baseline network. Since the MSD contains shape variations caused by atypical lesions, and thus the MSD-based ASM model has lower cross-dataset modeling capability. As a result, we finally choice to train the ASM model for \mathcal{L}_{asm} using the NIH dataset.

TABLE IV
COMPARE STATE-OF-THE-ART METHODS ON THE NIH.

Methods	DSC(%)*	Precision(%)*	Recall(%)*
M. Li et al [29].	83.31 \pm 6.32	84.09 \pm 8.65	83.30 \pm 8.54
Y. Zhang et al [41].	84.47 \pm 4.36	-	-
D. Zhang et al [15].	84.90	-	-
H. Chen et al [42].	85.19 \pm 4.73	86.09 \pm 5.93	84.58 \pm 8.09
J. Li et al [43].	83.35 \pm 4.13	83.45 \pm 7.19	82.76 \pm 8.21
p. Hu et al [44].	85.49 \pm 4.77	-	-
H. Li et al [45].	85.70 \pm 4.10	87.40 \pm 5.20	84.80 \pm 7.50
F. Li et al [46].	87.57 \pm 3.26	86.63 \pm 3.70	89.55 \pm 4.03
Ours	91.00 \pm 1.33	91.26 \pm 2.83	91.89 \pm 2.77
C. Qui et al [47].	86.25 \pm 4.52	-	-
S. Dai et al [48].	89.89 \pm 1.82	89.59 \pm 1.75	91.13 \pm 1.48

* The results (measured by the DSC, Precision, Recall) of pancreas segmentation on the NIH dataset. "—" denotes that the corresponding results are not provided in the literature. Optimal results (described by mean \pm std) are shown in red bold.

D. Comparison with state-of-the-art methods

NIH dataset. We compare our model against state-of-the-art methods [15], [29], [41]–[46], [48] on the NIH dataset using four-fold cross-validation. As shown in Table IV, our

proposed model achieves the state-of-the-art Dice score of 91.00%, outperforming prior arts. The low standard deviation of 1.33 demonstrates robustness across different cases. Our model also maintains high precision and recall, highlighting its potential. The superior accuracy and robustness validate the effectiveness of our shape context memory module and ASM prior constraint module.

TABLE V
COMPARE STATE-OF-THE-ART METHODS ON THE MSD.

Methods	DSC(%) [*]	Precision(%) [*]	Recall(%) [*]
H. Chen et al [42].	76.60 ± 7.30	87.70 ± 8.30	69.20 ± 12.80
Y. Zhang et al [41].	82.74	-	-
D. Zhang et al [15].	85.56	-	-
J. Li et al [43].	85.65	-	-
W. Li et al [17].	88.52 ± 3.77	-	91.86 ± 5.06
Ours	92.25 ± 1.12	94.79 ± 3.25	92.77 ± 1.88
Transform-Based S. Dai et al [48].	91.22 ± 1.37	93.22 ± 2.79	91.35 ± 1.63

^{*} The results (measured by the DSC, Precision, Recall) of pancreas segmentation on the MSD dataset. “—” denotes that the corresponding results are not provided in the literature. Optimal results (described by mean ± std) are shown in red bold.

MSD dataset. Table V shows the comparison of the proposed network with SOTA methods [15], [17], [41]–[43], [48] on the MSD. From Table V we can see that our network achieves a superior DSC of 92.25 %. The state-of-the-art results demonstrate the robustness of our proposed network.

V. CONCLUSION

To address the challenges of boundary ambiguity and large shape variations in pancreas segmentation, we propose a novel framework that consists of multi-scale Feature Extraction Module (MFE), mixed-scale attention integration module (MAI), shape context memory module (SCM), and a ASM prior constraint module, which combines the idea of multi-scale feature extraction and anatomical shape prior. Specifically, MFE and MAI are employed to solve the edge blur problem of the pancreas and obtain a reasonable pancreas region; the SCM implicitly encodes spatial and shape cues, in conjunction with the ASM prior constraint module, to guide shape-aware segmentation. Extensive experiments demonstrate the state-of-the-art performance and validate the efficiency of the SCM and ASM prior constraint components through ablation studies. Furthermore, our framework provides a generalizable approach for other medical image segmentation tasks. In future work, we will further investigate its application to other organ segmentation problems.

ACKNOWLEDGMENT

This work was supported by the National Natural Science Foundation of China under Grant 82261138629; Guangdong Basic and Applied Basic Research Foundation under Grant 2023A1515010688 and 2021A1515220072; Shenzhen Municipal Science and Technology Innovation Council under Grant JCYJ20220531101412030 and JCYJ20220530155811025.

REFERENCES

- [1] P. Ghaneh, E. Costello, and J. P. Neoptolemos, “Biology and management of pancreatic cancer,” *Postgraduate medical journal*, vol. 84, no. 995, pp. 478–497, 2008.
- [2] Y. Liu, M. Feng, H. Chen, G. Yang, J. Qiu, F. Zhao, Z. Cao, W. Luo, J. Xiao, L. You *et al.*, “Mechanistic target of rapamycin in the tumor microenvironment and its potential as a therapeutic target for pancreatic cancer,” *Cancer letters*, vol. 485, pp. 1–13, 2020.
- [3] L. Song, H. Wang, and Z. J. Wang, “Bridging the gap between 2d and 3d contexts in ct volume for liver and tumor segmentation,” *IEEE Journal of Biomedical and Health Informatics*, vol. 25, no. 9, pp. 3450–3459, 2021.
- [4] N. Heller, F. Isensee, K. H. Maier-Hein, X. Hou, C. Xie, F. Li, Y. Nan, G. Mu, Z. Lin, M. Han *et al.*, “The state of the art in kidney and kidney tumor segmentation in contrast-enhanced ct imaging: Results of the kits19 challenge,” *Medical image analysis*, vol. 67, p. 101821, 2021.
- [5] M. Antonelli, A. Reinke, S. Bakas, K. Farahani, A. Kopp-Schneider, B. A. Landman, G. Litjens, B. Menze, O. Ronneberger, R. M. Summers *et al.*, “The medical segmentation decathlon,” *Nature communications*, vol. 13, no. 1, p. 4128, 2022.
- [6] X. Li, H. Chen, X. Qi, Q. Dou, C.-W. Fu, and P.-A. Heng, “H-denseunet: hybrid densely connected unet for liver and tumor segmentation from ct volumes,” *IEEE transactions on medical imaging*, vol. 37, no. 12, pp. 2663–2674, 2018.
- [7] C. Zhao, Y. Xu, Z. He, J. Tang, Y. Zhang, J. Han, Y. Shi, and W. Zhou, “Lung segmentation and automatic detection of covid-19 using radiomic features from chest ct images,” *Pattern Recognition*, vol. 119, p. 108071, 2021.
- [8] N. Bouteldja, B. M. Klinkhammer, R. D. Bülow, P. Droste, S. W. Otten, S. F. von Stillfried, J. Moellmann, S. M. Sheehan, R. Korstanje, S. Menzel *et al.*, “Deep learning–based segmentation and quantification in experimental kidney histopathology,” *Journal of the American Society of Nephrology: JASN*, vol. 32, no. 1, p. 52, 2021.
- [9] R. Pohle and K. D. Toennies, “Segmentation of medical images using adaptive region growing,” in *Medical Imaging 2001: Image Processing*, vol. 4322. SPIE, 2001, pp. 1337–1346.
- [10] J. Gao, B. Wang, Z. Wang, Y. Wang, and F. Kong, “A wavelet transform-based image segmentation method,” *Optik*, vol. 208, p. 164123, 2020.
- [11] D.-P. Fan, G.-P. Ji, M.-M. Cheng, and L. Shao, “Concealed object detection,” *IEEE transactions on pattern analysis and machine intelligence*, vol. 44, no. 10, pp. 6024–6042, 2021.
- [12] Y. Pang, X. Zhao, L. Zhang, and H. Lu, “Multi-scale interactive network for salient object detection,” in *Proceedings of the IEEE/CVF conference on computer vision and pattern recognition*, 2020, pp. 9413–9422.
- [13] Y. Pang, X. Zhao, T.-Z. Xiang, L. Zhang, and H. Lu, “Zoom in and out: A mixed-scale triplet network for camouflaged object detection,” in *Proceedings of the IEEE/CVF Conference on computer vision and pattern recognition*, 2022, pp. 2160–2170.
- [14] Z. Huang, H. Dai, T.-Z. Xiang, S. Wang, H.-X. Chen, J. Qin, and H. Xiong, “Feature shrinkage pyramid for camouflaged object detection with transformers,” in *Proceedings of the IEEE/CVF Conference on Computer Vision and Pattern Recognition*, 2023, pp. 5557–5566.
- [15] D. Zhang, J. Zhang, Q. Zhang, J. Han, S. Zhang, and J. Han, “Automatic pancreas segmentation based on lightweight dcnn modules and spatial prior propagation,” *Pattern Recognition*, vol. 114, p. 107762, 2021.
- [16] H. Chen, Y. Liu, and Z. Shi, “Fpf-net: feature propagation and fusion based on attention mechanism for pancreas segmentation,” *Multimedia systems*, vol. 29, no. 2, pp. 525–538, 2023.
- [17] W. Li, S. Qin, F. Li, and L. Wang, “Mad-unet: A deep u-shaped network combined with an attention mechanism for pancreas segmentation in ct images,” *Medical Physics*, vol. 48, no. 1, pp. 329–341, 2021.
- [18] A. Davradou, “Detection and segmentation of pancreas using morphological snakes and deep convolutional neural networks,” *arXiv preprint arXiv:2302.06356*, 2023.
- [19] Q. Yu, L. Xie, Y. Wang, Y. Zhou, E. K. Fishman, and A. L. Yuille, “Recurrent saliency transformation network: Incorporating multi-stage visual cues for small organ segmentation,” in *Proceedings of the IEEE conference on computer vision and pattern recognition*, 2018, pp. 8280–8289.
- [20] Y. Zhou, L. Xie, W. Shen, Y. Wang, E. K. Fishman, and A. L. Yuille, “A fixed-point model for pancreas segmentation in abdominal ct scans,” in *International conference on medical image computing and computer-assisted intervention*. Springer, 2017, pp. 693–701.

- [21] T. D. Tam and N. T. Binh, "Efficient pancreas segmentation in computed tomography based on region-growing," in *Nature of Computation and Communication: International Conference, ICTCC 2014, Ho Chi Minh City, Vietnam, November 24-25, 2014, Revised Selected Papers I*. Springer, 2015, pp. 332–340.
- [22] X. Shan, C. Du, Y. Chen, A. Nandi, X. Gong, C. Ma, and P. Yang, "Threshold algorithm for pancreas segmentation in dixon water magnetic resonance images," in *2017 13th International Conference on Natural Computation, Fuzzy Systems and Knowledge Discovery (ICNC-FSKD)*. IEEE, 2017, pp. 2367–2371.
- [23] N. Ostu, "A threshold selection method from gray-level histograms," *IEEE Trans SMC*, vol. 9, p. 62, 1979.
- [24] M. Erdt, M. Kirschner, K. Drechsler, S. Wesarg, M. Hammon, and A. Cavallaro, "Automatic pancreas segmentation in contrast enhanced ct data using learned spatial anatomy and texture descriptors," in *2011 IEEE International Symposium on Biomedical Imaging: From Nano to Macro*. IEEE, 2011, pp. 2076–2082.
- [25] K. Karasawa, M. Oda, T. Kitasaka, K. Misawa, M. Fujiwara, C. Chu, G. Zheng, D. Rueckert, and K. Mori, "Multi-atlas pancreas segmentation: atlas selection based on vessel structure," *Medical image analysis*, vol. 39, pp. 18–28, 2017.
- [26] J. Long, E. Shelhamer, and T. Darrell, "Fully convolutional networks for semantic segmentation," in *Proceedings of the IEEE conference on computer vision and pattern recognition*, 2015, pp. 3431–3440.
- [27] O. Ronneberger, P. Fischer, and T. Brox, "U-net: Convolutional networks for biomedical image segmentation," in *Medical Image Computing and Computer-Assisted Intervention—MICCAI 2015: 18th International Conference, Munich, Germany, October 5-9, 2015, Proceedings, Part III 18*. Springer, 2015, pp. 234–241.
- [28] S. Aydin, "Deep learning classification of neuro-emotional phase domain complexity levels induced by affective video film clips," *IEEE Journal of Biomedical and Health Informatics*, vol. 24, no. 6, pp. 1695–1702, 2019.
- [29] M. Li, F. Lian, and S. Guo, "Automatic pancreas segmentation using double adversarial networks with pyramidal pooling module," *IEEE Access*, vol. 9, pp. 140965–140974, 2021.
- [30] K. He, X. Zhang, S. Ren, and J. Sun, "Deep residual learning for image recognition," in *Proceedings of the IEEE conference on computer vision and pattern recognition*, 2016, pp. 770–778.
- [31] L.-C. Chen, G. Papandreou, I. Kokkinos, K. Murphy, and A. L. Yuille, "DeepLab: Semantic image segmentation with deep convolutional nets, atrous convolution, and fully connected crfs," *IEEE transactions on pattern analysis and machine intelligence*, vol. 40, no. 4, pp. 834–848, 2017.
- [32] E. H. Adelson, C. H. Anderson, J. R. Bergen, P. J. Burt, and J. M. Ogden, "Pyramid methods in image processing," *RCA engineer*, vol. 29, no. 6, pp. 33–41, 1984.
- [33] T.-Y. Lin, P. Dollár, R. Girshick, K. He, B. Hariharan, and S. Belongie, "Feature pyramid networks for object detection," in *Proceedings of the IEEE conference on computer vision and pattern recognition*, 2017, pp. 2117–2125.
- [34] S. Ren, K. He, R. Girshick, and J. Sun, "Faster r-cnn: Towards real-time object detection with region proposal networks," *Advances in neural information processing systems*, vol. 28, 2015.
- [35] X. Zhao, Y. Pang, J. Yang, L. Zhang, and H. Lu, "Multi-source fusion and automatic predictor selection for zero-shot video object segmentation," in *Proceedings of the 29th ACM international conference on multimedia*, 2021, pp. 2645–2653.
- [36] Z. Zhou, M. M. Rahman Siddiquee, N. Tajbakhsh, and J. Liang, "Unet++: A nested u-net architecture for medical image segmentation," in *Deep Learning in Medical Image Analysis and Multimodal Learning for Clinical Decision Support: 4th International Workshop, DLMIA 2018, and 8th International Workshop, ML-CDS 2018, Held in Conjunction with MICCAI 2018, Granada, Spain, September 20, 2018, Proceedings 4*. Springer, 2018, pp. 3–11.
- [37] D.-P. Fan, G.-P. Ji, T. Zhou, G. Chen, H. Fu, J. Shen, and L. Shao, "Pranet: Parallel reverse attention network for polyp segmentation," in *International conference on medical image computing and computer-assisted intervention*. Springer, 2020, pp. 263–273.
- [38] X. Qin, Z. Zhang, C. Huang, C. Gao, M. Dehghan, and M. Jagersand, "Basnet: Boundary-aware salient object detection," in *Proceedings of the IEEE/CVF conference on computer vision and pattern recognition*, 2019, pp. 7479–7489.
- [39] J. Wei, S. Wang, and Q. Huang, " F^3 net: fusion, feedback and focus for salient object detection," in *Proceedings of the AAAI conference on artificial intelligence*, vol. 34, no. 07, 2020, pp. 12321–12328.
- [40] H. R. Roth, L. Lu, A. Farag, H.-C. Shin, J. Liu, E. B. Turkbey, and R. M. Summers, "Deeporgan: Multi-level deep convolutional networks for automated pancreas segmentation," in *Medical Image Computing and Computer-Assisted Intervention—MICCAI 2015: 18th International Conference, Munich, Germany, October 5-9, 2015, Proceedings, Part I 18*. Springer, 2015, pp. 556–564.
- [41] Y. Zhang, J. Wu, Y. Liu, Y. Chen, W. Chen, E. X. Wu, C. Li, and X. Tang, "A deep learning framework for pancreas segmentation with multi-atlas registration and 3d level-set," *Medical Image Analysis*, vol. 68, p. 101884, 2021.
- [42] H. Chen, Y. Liu, Z. Shi, and Y. Lyu, "Pancreas segmentation by two-view feature learning and multi-scale supervision," *Biomedical Signal Processing and Control*, vol. 74, p. 103519, 2022.
- [43] J. Li, X. Lin, H. Che, H. Li, and X. Qian, "Pancreas segmentation with probabilistic map guided bi-directional recurrent unet," *Physics in Medicine & Biology*, vol. 66, no. 11, p. 115010, 2021.
- [44] P. Hu, X. Li, Y. Tian, T. Tang, T. Zhou, X. Bai, S. Zhu, T. Liang, and J. Li, "Automatic pancreas segmentation in ct images with distance-based saliency-aware denseapp network," *IEEE journal of biomedical and health informatics*, vol. 25, no. 5, pp. 1601–1611, 2020.
- [45] H. Li, J. Li, X. Lin, and X. Qian, "A model-driven stack-based fully convolutional network for pancreas segmentation," in *2020 5th International Conference on Communication, Image and Signal Processing (CCISP)*. IEEE, 2020, pp. 288–293.
- [46] F. Li, W. Li, Y. Shu, S. Qin, B. Xiao, and Z. Zhan, "Multiscale receptive field based on residual network for pancreas segmentation in ct images," *Biomedical Signal Processing and Control*, vol. 57, p. 101828, 2020.
- [47] C. Qiu, Z. Liu, Y. Song, J. Yin, K. Han, Y. Zhu, Y. Liu, and V. S. Sheng, "Rtunet: Residual transformer unet specifically for pancreas segmentation," *Biomedical Signal Processing and Control*, vol. 79, p. 104173, 2023.
- [48] S. Dai, Y. Zhu, X. Jiang, F. Yu, J. Lin, and D. Yang, "Td-net: Trans-deformer network for automatic pancreas segmentation," *Neurocomputing*, vol. 517, pp. 279–293, 2023.